Digest Journal of Nanomaterials and Biostructures

Dig. J. Nanomater. Bios. **2026**; 21(3): 57847
https://doi.org/10.31083/DJNB57847

Original Research

Carbon Nitride as a Platform for Sulphur-Containing Pollutant Sensing: A Density Functional Theory Study on Sulphur Mustard and Minoxidil

Javed Iqbal[1,*], Hina Ahmed[2], Hafsa Nadeem[2], Khurshid Ayub[3], Shaimaa A. M. Abdelmohsen[4,*], Haifa A. Alyousef[4]

[1]Department of Chemistry, College of Science, University of Bahrain, 32038 Sakhir, Kingdom of Bahrain
[2]Department of Chemistry, University of Agriculture, 38000 Faisalabad, Pakistan
[3]Department of Chemistry, COMSATS University, Abbottabad Campus, 22010 Islamabad, Pakistan
[4]Department of Physics, College of Science, Princess Nourah bint Abdulrahman University, 11671 Riyadh, Saudi Arabia
*Correspondence: Javedkhattak79@gmail.com; Jiqbal@uob.edu.bh (Javed Iqbal); shamohamed@pnu.edu.sa (Shaimaa A. M. Abdelmohsen)
Academic Editor: Giuseppe Trusso Sfrazzetto
Submitted: 12 February 2026 Revised: 3 May 2026 Accepted: 5 June 2026 Published: 11 September 2026

Abstract

Background: Carbon nitride (C_6N_8) holds promise as a two-dimensional nanomaterial for chemical sensing because of its advantageous electronic properties, high surface area, and structural stability. **Method:** The suitability of C_6N_8 for the adsorptive sensing of sulphur mustard ($C_4H_8Cl_2S$) and minoxidil ($C_9H_{15}N_5O$) was investigated using density functional theory calculations at the B3LYP/6-31G(d,p) level. The sensing mechanism and adsorption behavior were explored through interaction energy calculations and frontier molecular orbital, density of states, natural bond orbital (NBO), molecular electrostatic potential mapping, electron localization function (ELF), quantum theory of atoms in molecules (QTAIM), and noncovalent interaction (NCI) analyses. **Results:** The calculated adsorption energies of sulphur mustard and minoxidil (−30.39 and −85.34 kJ mol^{-1}, respectively) indicated favorable adsorption, with minoxidil exhibiting stronger interactions with the C_6N_8 surface. Upon the adsorption of sulphur mustard and minoxidil, the bandgap of C_6N_8 decreased from 4.206 to 4.007 and 3.067 eV, respectively. Charge transfer between the adsorbates and sensing surface, together with hydrogen bonding, van der Waals interactions, and steric effects, was confirmed by NBO, NCI, ELF, and QTAIM analyses. **Conclusion:** C_6N_8 exhibits excellent sensitivity toward both analytes and can serve as a promising sensing platform for the detection of hazardous sulphur-containing pollutants and pharmaceutical contaminants. The results provide valuable theoretical insights for the development of advanced nanosensor technologies.

Keywords: minoxidil; noncovalent interaction; molecular electrostatic potential; density of states; electron localization function; sulphur mustard

1. Introduction

The fast development of chemical technology is causing the release of many harmful gases that are extremely dangerous for both humans and other living organisms on Earth. A variety of organic and inorganic compounds are used to save the environment from global warming [1,2,3]. Several kinds of carbon nitride membranes have been suggested by scientists. However, C_6N_8 monolayers were the most interesting among them. Due to the astounding experimental advancements made in their synthesis, nanomaterials made of this double carbon nitride (2D-CN) have recently gained a lot of attention [4]. A variety of materials, such as graphene, covalent compounds, and activated C (2D materials), are used as a sensing surface for different gases. The high surface area of C_6N_8 monolayers for chemical reactions is the main reason for selecting it as a sensor surface for this study. In C_6N_8 monolayers, the N-atom has more charge dominance than the C-atom due to two reasons: first, it is the presence of sp_2 hybridisation between them, and second, it is the high electronegativity of the N-atom. The embedding of atomic effects on the C_6N_8 monolayers has a major impact on their electronic and magnetic properties, resulting in unusual and diverse electronic properties, including mineral, half-metallic, spin-glass semiconductor, and dilute-magnetic semiconductor [5].

Due to their photocatalysis and associated applications, allotropes of carbon nitride (CN) have continued to be the subject of substantial basic and applied research. The CN allotropes are derived from the chemical formula C_pN_q, where p and q denote the number of C and N atoms in the CN unit cell. At ambient temperature, the heptazine (C_6N_8) sheet is typically the most stable of all the others. Additionally, the C_6N_8 band gap (2.7 eV) has been synthesized for a very long time into a monolayer form [6] and is excellent for studying the visible portion of the solar spectrum. Due to their size-dependent band gaps, carbon nitride nanotubes have recently been described as promising materials for solar energy absorbers. The carbon nitride allotrope C_6N_8's photoactivity can be raised by adding nonmetal atoms and a doping process, and after the functionalization procedure,

the allotrope's ability to absorb visible light has also risen [7]. Doping of C_6N_8 and C_6N_6 monolayers with different kinds of atoms (metal and non-metal) enhances their electronic properties by converting them into magnetic-non-magnetic materials [8]. Various types of electronic properties, such as half-metallic, metallic, dilute semiconductor, and spin-glass semiconductor, of C_6N_8 can be affected by the doping of various metals, such as Mg, C, and Cr [5]. C_6N_8 is the most stable and widely accessible allotrope [9]. During harsh conditions, it shows chemical and thermal stability, which makes it the most authentic molecule used as a sensor [10]. In this way, doped carbon-based nanomaterials can be used in different technologies.

Since its debut distribution as a chemical agent in World War I, sulphur mustard has been utilized often in a number of military confrontations. Furthermore, the accidental exposure to sulphur mustard has been linked to several injuries, and post-war chemical weapons are still exceedingly dangerous [11]. However, there is now no medication or cure that can stop the fundamental cause of harm from sulphur mustard. Furthermore, sulphur mustard is the most likely harmful substance due to its straightforward composition and quick manufacturing. The development of sulphur mustard and its analogues detection techniques is therefore crucial. Fluorescent chemosensors stand out among the many detection techniques thanks to their remarkable benefits, such as affordability, ease of use, and great selectivity [12]. Sulphur Mustard is actually an oily liquid of relatively low volatility at temperatures that are appropriate for the environment. While operational sulphur mustard is dark and has a faint garlic aroma, pure sulphur mustard is colourless and odourless [13].

Strong vesicants like sulphur mustard may harm the respiratory system, produce eye sores, blister the skin, and depress the bone marrow. Long-term exposure to sulphur mustard can have carcinogenic and mutagenic consequences because it can react with DNA's guanine nucleotide as an alkylating agent. It should be noted that following exposure to sulphur mustard, patients typically undergo an incubation period of between 30 minutes and eight hours before symptoms manifest. As a result, the response process is typically delayed, leading to greater harm [14]. Another alkylating substance is sulphur mustard, which may alkylate proteins, DNA, glutathione (GSH), and other biomolecules. The primary toxicological pathways of sulphur mustard are linked to DNA damage brought on by alkylation and oxidative stress brought on by glutathione depletion [15]. The burn produced by nitrogen mustards is often less severe than the burn induced by sulphur mustard, and infections frequently lead to vesication before sulphur mustard. Despite the fact that burns produced by mustards can hold patients in the hospital for weeks, deaths from sulphur mustard in wars have been rare, generally only occurring after victims had inhaled very large amounts of vapour [16].

Minoxidil is a vasodilator, which relaxes (widens) blood vessels and enhances blood flow. It is used to treat resistant patients with hypertension. Liquid retention and hirsutism should occur in patients who get this medication in excess by oral administration. Dermatology has a novel use for minoxidil, particularly in the treatment of pattern baldness. For the determination of minoxidil, a number of techniques have been published, including ultraviolet–visible (UV–vis), fluid injection with photometric [17], or liquid chromatography photometric titrations and spectrophotometry, along with polarography.

Currently, minoxidil is used to treat alopecia areata and male pattern baldness (alopecia androgenica). Not long ago, Brett and his colleagues found a detection limit of 1.35 M for the oxidation process of minoxidil at 0.86 V and pH 2 on carbon black resin and carbon black paste electrodes. In other contexts, in order to quantify the concentration of minoxidil in pH 2 using differential pulse voltammetry (DPV) with a limit of detection (LOD) of 0.01 M, an electropolymerized molecularly imprinted polymer was utilized [18].

The 2% product was originally offered for men's hair regrowth in 1986, while the 5% product was made available in 1993 [19]. By electro-polymerizing functional monomers of o-phenylenediamine, co-gallic acid, and p-aminobenzoic acid, a minoxidil sensor was created. The functionalization of molecular imprinted polymers for minoxidil as the target molecule was accomplished using a computational method based on density functional theory (DFT) [20]. The square wave voltammetry-based selective extraction of minoxidil in the modified electrode provides the basis for the detection process. The made-to-order sensor has been used successfully to identify minoxidil in actual samples. The square wave voltammetry-based selective extraction of minoxidil in the electrode surface provides the basis for the detection process. The created sensor has been used favorably to identify minoxidil in actual specimens [21].

Carbon nitride (C_6N_8), as a nanosensor, works efficiently because of its semiconductor nature. The monolayer of C_6N_8 by transfer charges can act as a donor or acceptor, which is determined by charge transfer analysis [22]. By adsorption of various gas molecules, the charge density of Carbon nitride (C_6N_8) increases, which makes it a highly sensitive sensor [23]. It has great potential as a sensor for detecting different types of gases. The large surface area and high stability make it a good sensor. We can also modify its electrical properties by incorporating other atoms. It can also be synthesized in the laboratory.

Herein, This study hypothesizes that the C_6N_8 nanosheet exhibits significantly different adsorption and electronic responses toward sulphur mustard and minoxidil, enabling selective detection of sulphur mustard through favorable adsorption characteristics and pronounced changes in its electronic properties.

2. Materials and Methods

Quantum chemical calculations were performed using Gaussian 09 (Revision D.01, Gaussian, Inc., Wallingford, CT, USA). Molecular structures, input preparation, and visualization of Gaussian results were carried out using GaussView 6.0 (Gaussian, Inc.). Wavefunction analyses were conducted using Multiwfn 3.8 (developed by Tian Lu, Beijing Kein Research Center for Natural Sciences, Beijing, China; website: http://sobereva.com/multiwfn). Molecular orbital and electrostatic potential isosurfaces were rendered using Visual Molecular Dynamics (VMD) 1.9.3 (Theoretical and Computational Biophysics Group, Beckman Institute for Advanced Science and Technology, University of Illinois at Urbana–Champaign, Urbana, IL, USA; website: https://www.ks.uiuc.edu/Research/vmd/). Using the B3LYP/6-31G(d,p) optimization of structures, energy calculations, and analysis of natural bond orbitals (NBO), and DOS were carried out. According to literature, B3LYP is an appropriate and reliable density function for estimating the optical, energetic, physical, and electrical properties of diverse nanomaterials [9].

Density states were used to determine the number of electron states per volume at a specific energy. Using VMD, the isosurfaces of the NCI and quantum theory of atoms in molecules (QTAIM) analyses were shown, and the reduced density gradient (RDG) scattering images of the NCIs were displayed. To acquire a sense of NCIs, RDG plots and 3D isosurfaces were used. Additionally, utilizing QTAIM analysis to determine the bond critical point, the NCIs between C_6N_8 and analytes were measured [24].

To look at the conductivity and interactions of the analyte@C_6N_8 complexes, the DOS of the most stable geometries was analyzed. A DOS evaluation was carried out to have a thorough understanding of the number of states that electrons can occupy at a given energy level. The highest occupied molecular orbital (HOMO)/lowest unoccupied molecular orbital (LUMO) region underwent modifications, and the energy states that were available provided insight into how complexation affected the electrical characteristics and sensing capabilities of C_6N_8. To look at the conductivity and interactions of the analyte@C_6N_8 complexes, the DOS of the most reliable systems was analyzed. To gain a thorough understanding of the different states that electrons can occupy at a given energy level, DOS analysis was carried out. The energy states that were accessible helped us to comprehend the alterations that were placed in the HOMO/LUMO region [24]. The output files of all the methods are shown through the GaussView software [25]. The activity indicators on a worldwide scale are computed. Based on Eqn. 1, the chemical potential is clearly determined.

$$\mu = -\left(E_{HOMO} + E_{LUMO}\right)/2 \tag{1}$$

E_{HOMO} stands for the energy of the HOMO in this instance, while E_{LUMO} stands for the energy of the LUMO [26].

Softness (S) and electrophilicity (ω) are quantified as follows: Eqns. 2,3.

$$S = 1/(2\eta) \tag{2}$$

$$\omega = \mu^2/2\eta \tag{3}$$

3. Results

C_6N_8 was tested as an adsorbent material for sulphur mustard and minoxidil using DFT simulations. The DFT method gives better results; therefore, choose the DFT method for further experiments. The optimized structure of C_6N_8 is used as a surface for sulphur mustard and minoxidil. Fig. 1 represents the front and side images of the optimized geometry of the surface. The optimized structures of analytes $C_4H_8Cl_2S$ and $C_9H_{15}N_5O$ are more preferred by the DFT method, as shown in Fig. 2.

3.1 Interaction Energies

The interaction energy of sulphur mustard and minoxidil over C_6N_8 was calculated by the following formula:

$$E_{\text{int}} = E_{\text{complex}} - \left(E_{\text{analyte}} + E_{\text{surface}}\right) \tag{4}$$

3.2 UV Properties

The presence of many peaks in the UV graph through Origin denotes the existence of excited electrons. The larger the wavelength that is absorbed, the easier it is to absorb additional electrons [27]. The absorbance increases as more electrons are taken in. The UV graph through Origin gives information about the maximum absorbance [28].

3.3 Non-Covalent Interactions

3.3.1 3D Isosurface

The analysis of Visual Molecular Dynamics was carried out using Multiwfn software. The simulation results were analysed by using visual molecular dynamics analysis. If the green patches are present between the surface and analyte, then it shows the Van der Waals forces or dispersion interactions. If the light blue color is present, it represents the hydrogen bonding, and the red color shows the repulsive forces.

3.3.2 Electron Localization Function (ELF)

ELF was developed by Becke and Edgecombe on the basis of a provisional identical pair density function, which supports the use of density functional theory-based tech-

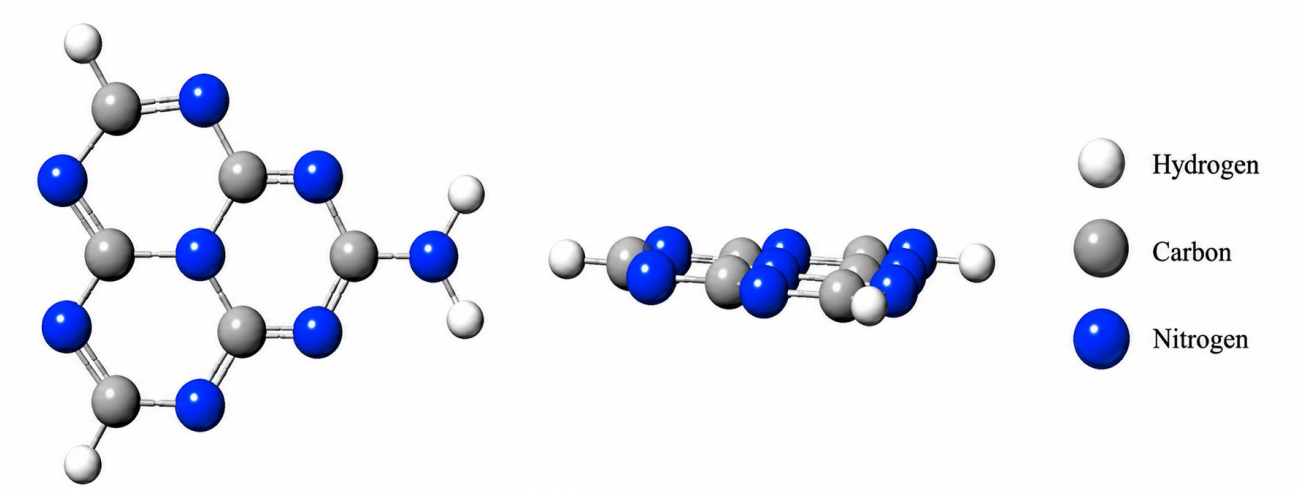

Fig. 1. Front and side images of optimized geometry of the C_6N_8 Surface.

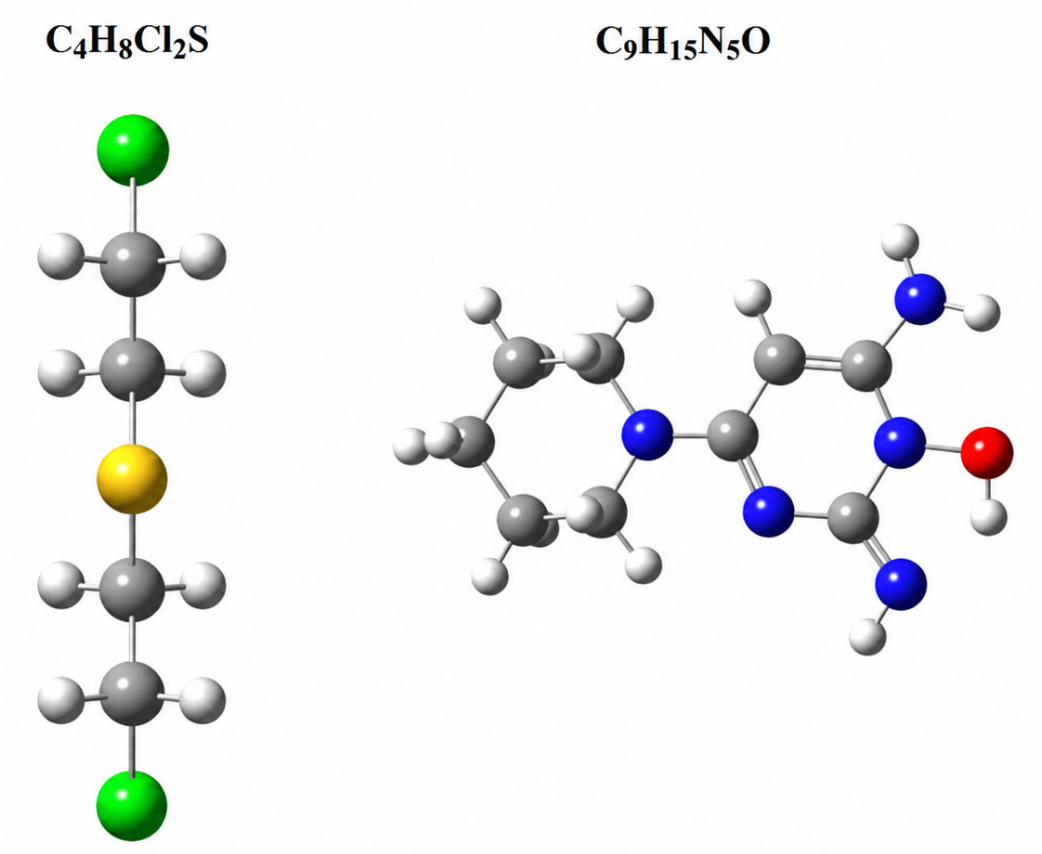

Fig. 2. Optimized structure of $C_4H_8Cl_2S$ and $C_9H_{15}N_5O$ analytes.

niques to calculate ELF. ELF was established on the thermal density of electrons [29]. ELF shows a high prospect of detecting a pair of electrons on the face of the molecule, achieved by the Multiwfn software [30]. The ELF graph is considered in the range between 0.0 and 1.0. Area below 0.5 describes a delocalized electron region. If the plotted value of ELF is in the range of 0.5 to 1.0, then the electrons are both localized and bonded; if it is in a range of 0.5, then the electrons are delocalized [31]. More red color is present in the ELF graph of the surface, which stands for strong electronic localization.

3.4 QTAIM Analysis

In $C_4H_8Cl_2S@C_6N_8$, four types of bond critical points appear, such as 43, 59, 61, and 70 in Fig. 3. In Table 1, positive values of Laplacian electron density indicate the presence of non-covalent interaction, and negative values show the ionic interaction [32].

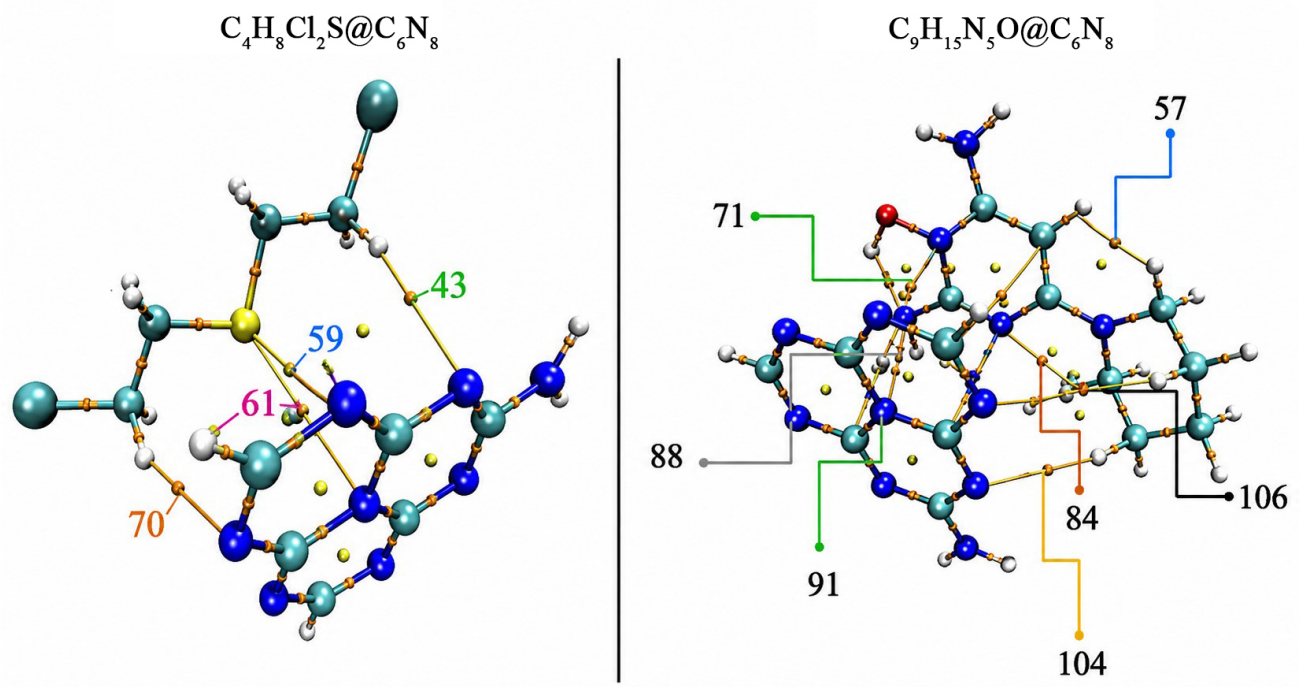

Fig. 3. QTAIM analysis of complexes $C_4H_8Cl_2S@C_6N_8$ and $C_9H_{15}N_5O@C_6N_8$. QTAIM, quantum theory of atoms in molecules.

Table 1. Values of BCPs (laplacian of electron density $\nabla^2\rho$, potential electron energy density V(r), kinetic electron energy G(r), electron density (ρ), and total electron energy density [H(r)]) of $C_4H_8Cl_2S@C_6N_8$ complex obtained from QTAIM analysis.

BCP	A int	(ρ)	$\nabla^2\rho$	G(r)	V(r)	H(r)
43	N9...H30	0.007	0.023	0.004	–0.004	0.0007
59	N12...S21	0.003	0.012	0.002	–0.001	0.0005
61	N11...S21	0.004	0.011	0.002	–0.002	0.0004
70	N14...H33	0.006	0.019	0.004	–0.003	0.0006

BCPs, bond critical points; A int, interaction energy; QTAIM, quantum theory of atoms in molecules.

In $C_9H_{15}N_5O@C_6N_8$, seven types of bond critical points are observed as shown in Table 2. Only two types of bond critical points are observed, such as 57 and 71. Bonds between connected atoms are observed by negative values of $\nabla^2\rho$ and H(r), which designate the covalent interaction [33].

3.5 Recovery Time of Surface C_6N_8

One of the main factors in determining if C_6N_8 is an appropriate gas sensor is calculating the recovery time for analyte desorption. Recovery time tells us about the stability of the complex and the sensing ability of the surface. Conceptual model, using the transition state concept, recovery periods (s) for the desorption of $C_4H_8Cl_2S$ and $C_9H_{15}N_5O$ were determined, which can be indicated as:

$$\tau = \upsilon^{-1} e^{-\mathrm{Eads/KT}} \quad (5)$$

T represents the system's temperature, and υ indicates attempt frequency. According to the transition theory, recovery time elongates as adsorption energy E_{ad} rises. Where K shows the Boltzmann constant (8.62×10^{-5} eV K^{-1}). At ambient temperature, recovery time increases when the adsorption energy is greater than 1.0 eV, and the sensor takes more than 12 h to recover. At 300 K, the recovery time for $C_4H_8Cl_2S@C_6N_8$ and $C_9H_{15}N_5O@C_6N_8$ is observed in Table 3.

4. Discussion

4.1 Interaction Energies

The interaction energies and interaction distances of sulphur mustard and minoxidil adsorbed on the C_6N_8 surface are observed in Table 3. If the molecule has more interaction energy, then this molecule is more stable. The least H-23…N-44 adsorption distance, which is 2.639 Å, indicates that the $C_9H_{15}N_5O@C_6N_8$ complex has the highest stability. $C_4H_8Cl_2S@C_6N_8$ shows the interaction energy −30.39 kJ mol^{-1}. The highest interaction energy is −85.34 kJ mol^{-1} observed for $C_9H_{15}N_5O@C_6N_8$ due to the conjunction and efficient overlapping of orbitals. Adsorption energy less than 1 eV indicates the physisorption process between the analyte and the surface. The high adsorption energy value of $C_9H_{15}N_5O@C_6N_8$ complex represents the physisorption process [22]. The technique of the adsorp-

Table 2. Values of BCPs (laplacian of electron density $\nabla^2\rho$, potential electron energy density V(r), kinetic electron energy G(r), electrondensity (ρ), and totalelectron energy density [H(r)]) of $C_9H_{15}N_5O@C_6N_8$ complex obtained from QTAIM analysis.

BCP	A int	(ρ)	$\nabla^2\rho$	G(r)	V(r)	H(r)
57	C2...N14	0.3647	–1.3246	0.2425	–0.8162	–0.5737
71	N21...C20	0.1710	–0.2604	0.0453	–0.1558	–0.1105

Table 3. Interaction energies (kJ mol^{-1}) and interaction distances (Å) of optimized complexes.

Complex	$E_{kJ\ mol}{}^{-1}$	Closest interacting atoms	$D_{INT(Å)}$	$Q_{NBO(e-)}$	Recovery time of the sensor (s)	BSSE energy (eV)
$C_4H_8Cl_2S@C_6N_8$	–30.39	N9...H30	2.643	–0.088	1.001×10^{-12}	0.0828
$C_9H_{15}N_5O@C_6N_8$	–85.34	H23...N44	2.639	-8×10^{-3}	7.749×10^{46}	0.1846

INT, interaction energy; NBO, natural bond orbital; BSSE, basis set superposition error.

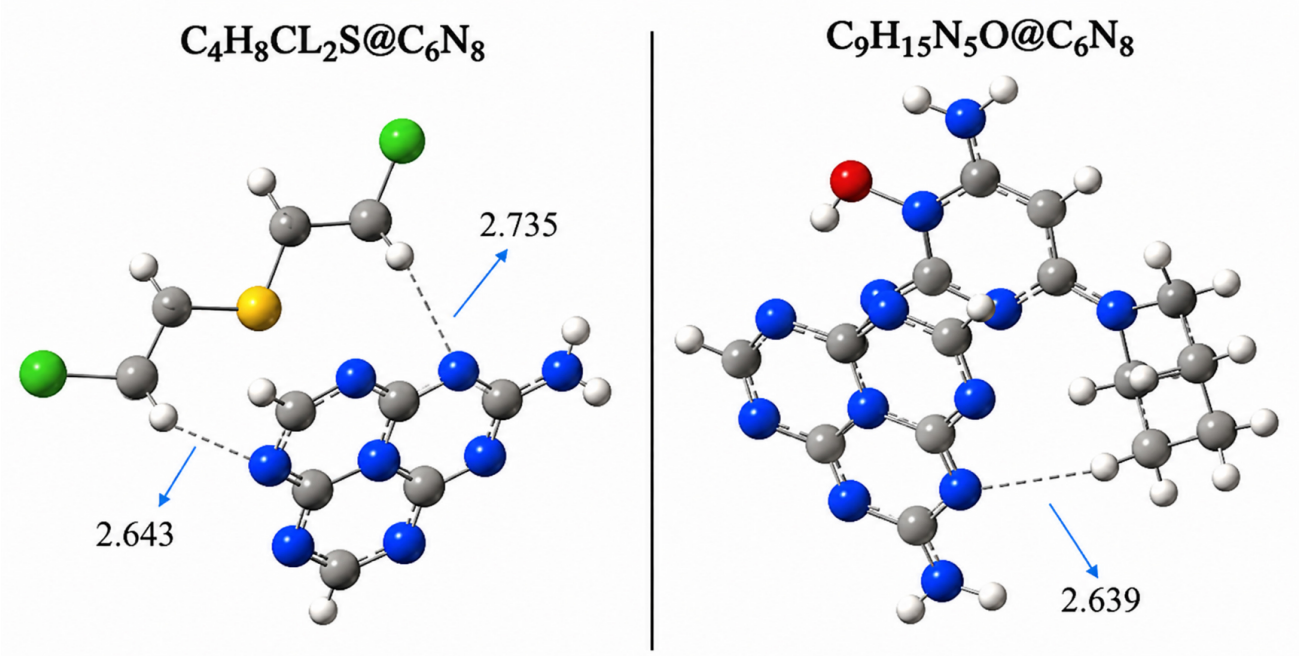

Fig. 4. Optimized structure of complexes $C_4H_8Cl_2S@C_6N_8$ and $C_9H_{15}N_5O@C_6N_8$.

tion process was corroborated by the results of the binding energy of the analytes and complex [34].

Higher interaction energy shows the stability of the complex [35]. Fig. 4 shows the closest interacting distance in optimized geometries of complexes $C_4H_8Cl_2S@C_6N_8$ and $C_9H_{15}N_5O@C_6N_8$. Basis set superposition error (BSSE) energy for $C_4H_8Cl_2S@C_6N_8$ is 0.0828 and for $C_9H_{15}N_5O@C_6N_8$ is 0.1846 in Table 3. A small basis set stabilizes the complex due to BSSE energy.

4.2 FMO Analysis

Several other electronic characteristics were computed, including the power of the highest occupied molecular orbital (E_{HOMO}) and the lowest unoccupied molecular orbital (E_{LUMO}). Koopman's theorem states that the ionization potential (I) of molecules and the electron affinity (A) are linked to the E_{HOMO} and E_{LUMO} [36]. When the objective molecule with the high HOMO energy serves as the electron carrier and the associated molecule as the acceptor with the lower LUMO energy, the interaction is strengthened. The chemical's kinetic persistence and high reactivity are described by the universal reactivity parameters [37].

Frontier molecular orbitals (FMOs), which are the LUMO and the HOMO, respectively, are critical for chemical procedures as well as electrical and optical achievement. HOMO and LUMO of $C_4H_8Cl_2S@C_6N_8$ and $C_9H_{15}N_5O@C_6N_8$ are represented in Fig. 5. HOMO has the capacity to donate an electron, and LUMO has the capacity to receive an electron. Moreover, the "energy band gap" refers to the energy gaps between HOMO and LUMO. The energy gap values of HOMO-LUMO affect the chemical strength and bioactive molecule (Fig. 6).

The band gap of surface C_6N_8 is 4.206 eV. With the complexation of analytes with the surface, the band gaps of $C_4H_8Cl_2S@C_6N_8$ and $C_9H_{15}N_5O@C_6N_8$ are 4.007eV and 3.067 eV, respectively, as observed in Table 4. A few alterations in the band gap of surface C_6N_8 are seen on the adsorption of sulphur mustard and minoxidil, suggest-

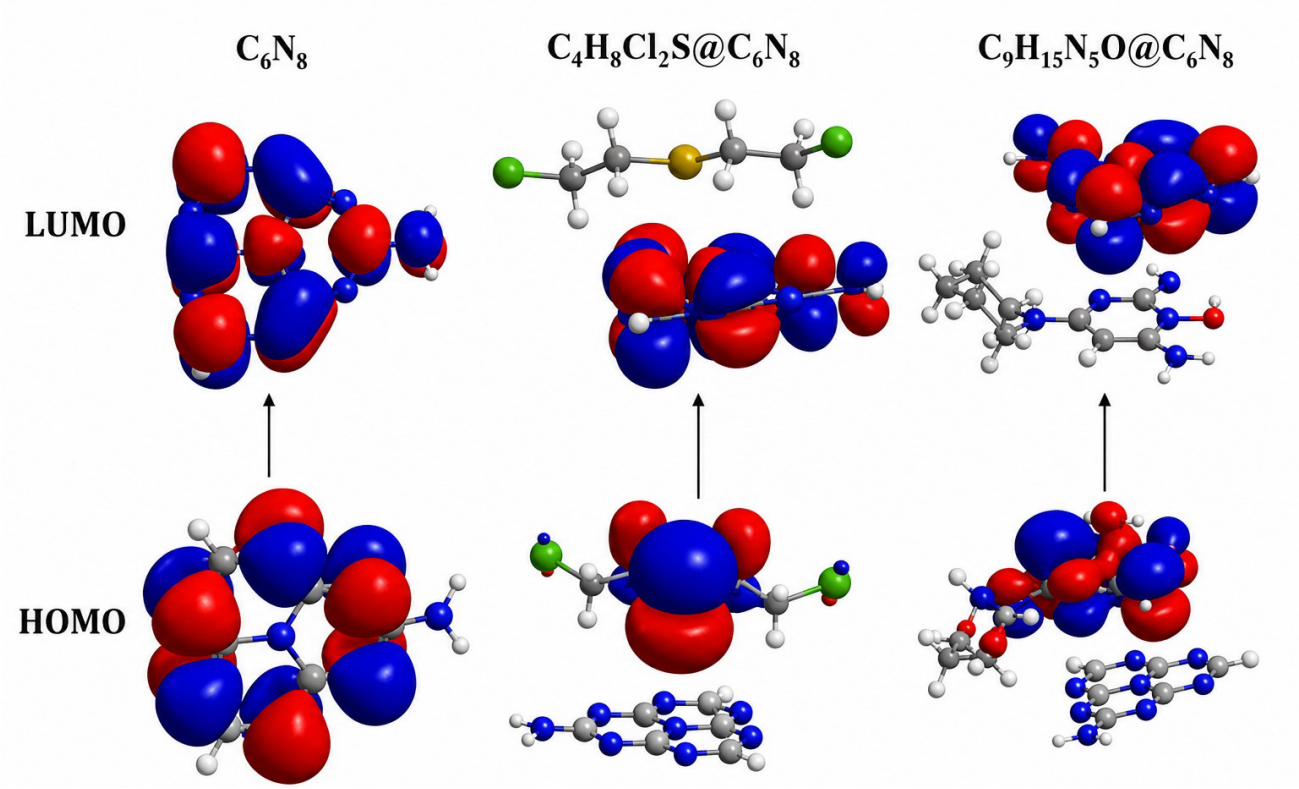

Fig. 5. HOMO and LUMO of C_6N_8, $C_4H_8Cl_2S@C_6N_8$, and $C_9H_{15}N_5O@C_6N_8$.

Table 4. FMO analysis and values of softness (S), hardness (η), chemical potential (μ), and electrophilicity (ω) of Analyte@C_6N_8 Complexes.

Molecules	E_{HOMO} (eV)	E_{LUMO} (eV)	Energy gap (eV)	Softness (eV^{-1})	Hardness (eV)	Chemical potential (eV)	Electrochemical potential (eV)
C_6N_8	–6.671	–2.464	4.206	0.092	5.439	4.567	1.917
$C_4H_8Cl_2S$	–6.594	–0.226	6.368	0.077	6.481	3.410	1.003
$C_9H_{15}N_5O$	–5.105	0.070	5.175	0.099	5.07	2.5175	1.468
Complex 1	–6.620	–2.613	4.007	0.094	5.313	4.616	2.005
Complex 2	–5.175	–2.107	3.067	0.122	4.122	3.641	1.608

FMO, frontier molecular orbital; HOMO, highest occupied molecular orbital; LUMO, lowest unoccupied molecular orbital.

ing irregular interactions between the surface and the analytes. Maximum hardness shows the greater stability of the molecule. Different types of parameters are shown in Fig. 7.

Natural Bond Orbital Analysis

Natural bond orbital analysis is used to investigate the intermolecular and intramolecular charge transfer. Quantum natural bond orbital (QNBO) analysis is used to investigate the charge transfer between analytes and the surface during interaction. Positive value of QNBO shows the transfer of charge from analyte to surface, and a negative value shows the transfer of charge from surface to analyte. The negative values of both complexes show the charge transfer from the surface to the analyte. Both complexes show the positive values of QNBO, which indicate that charges are transferred from the surface (C_6N_8) to the anlyte in both complexes due to the high density of electrons on the surface [22]. The value of QNBO in $C_4H_8Cl_2S@C_6N_8$ is –0.088 and in $C_9H_{15}N_5O@C_6N_8$ is -8×10^{-3} in Table 3.

4.3 UV Adsorption Properties

In Fig. 8, $C_4H_8Cl_2S@C_6N_8$ shows the adsorption value of 270 nm supporting π→π∗, and $C_9H_{15}N_5O@C_6N_8$ shows the λmax of 400 nm. The graph of $C_4H_8Cl_2S@C_6N_8$ complex goes into the Ultraviolet region because this region has the wavelength in the range of 100–400 nm. The graph of $C_9H_{15}N_5O@C_6N_8$ complex goes into the visible region because this region has the wavelength range 400–800 nm.

4.4 Non-Covalent Interactions

NCIs have a distinctive signature, and the electron density is the only way to detect their presence. The RDG

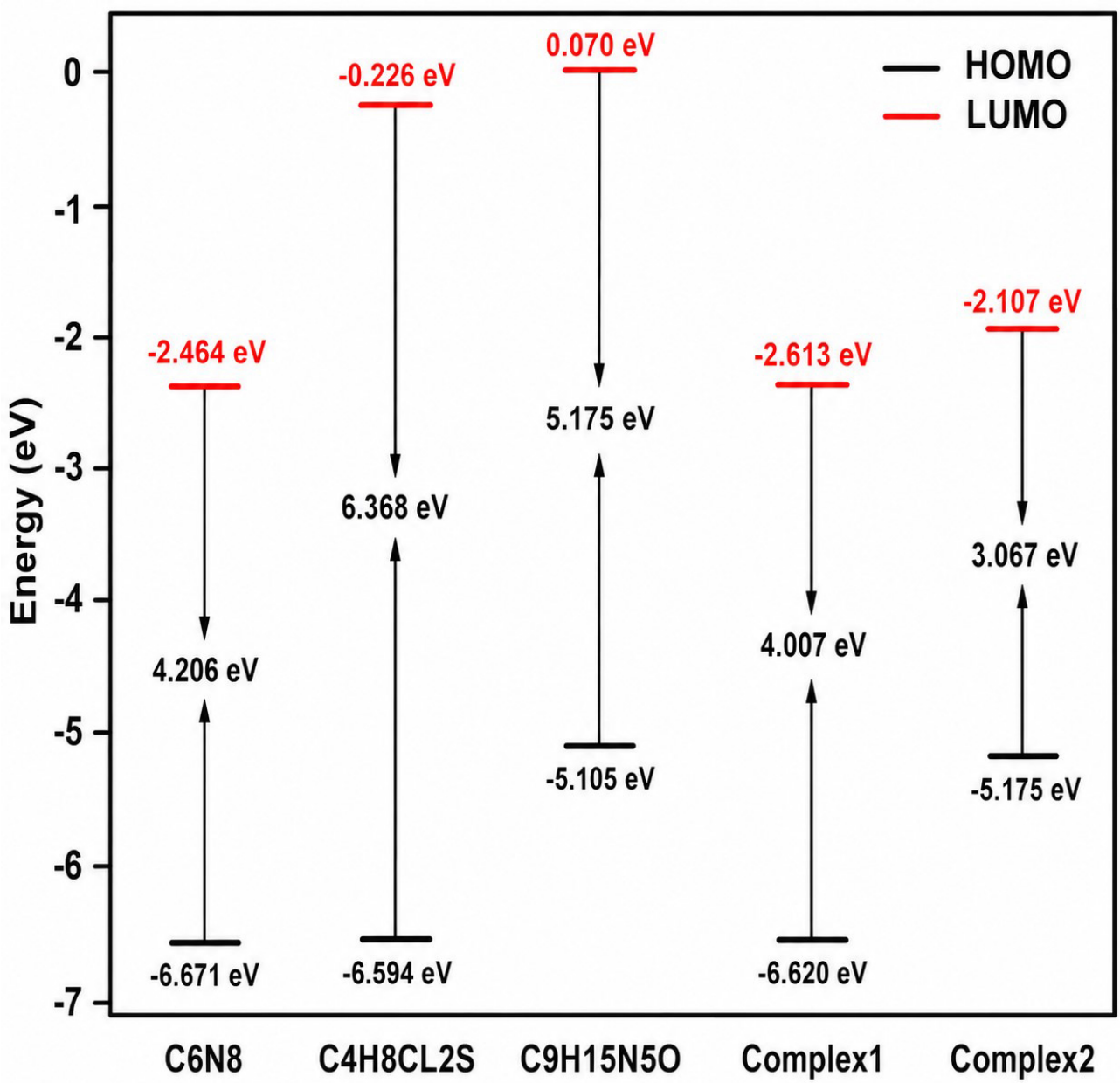

Fig. 6. Graphical representation of HOMO, LUMO, and energy gap values in eV.

approach has been used to examine various NCI kinds in real space. Under the context of DFT, the RDG, a basic immeasurable function of the electron density gradient standard, is utilized to explain the departure from a uniform electron distribution to non-uniform electron density [34]. The color coding for the depiction of NCI iso-surfaces is as follows: blue denotes attractive interactions, red denotes repulsive interactions, and green denotes intermediate interactions. The presence of a darker hue in the graph represents the stronger forces between the anlyte and the surface [38]. Greater molecular complexes may be described using the NCI indices at a cheap computing expense and with informative findings by using a promolecular density [39]. The electrostatic impact, which appears as a red circle on the isosurface of all the benzene rings, is caused by the spike around +0.020 a.u [40].

In Fig. 9 of $C_4H_8Cl_2S@C_6N_8$ thin spikes of green color show weak dispersive interactions according to Van der Waals forces, and thick spikes of red color stand for the strong steric repulsion present in the complex. In Fig. 9 of $C_9H_{15}N_5O@C_6N_8$ blue color expresses the strong hydrogen bond, the green color appears for the interactions according to Van der Waals (dispersion force), and the red color represents the strong steric repulsion. In this graph, red and blue colors are more dense.

The more particular approach, known as lowered density gradient research, is applied to produce the noncovalent coupling more precisely. The RDG analysis was

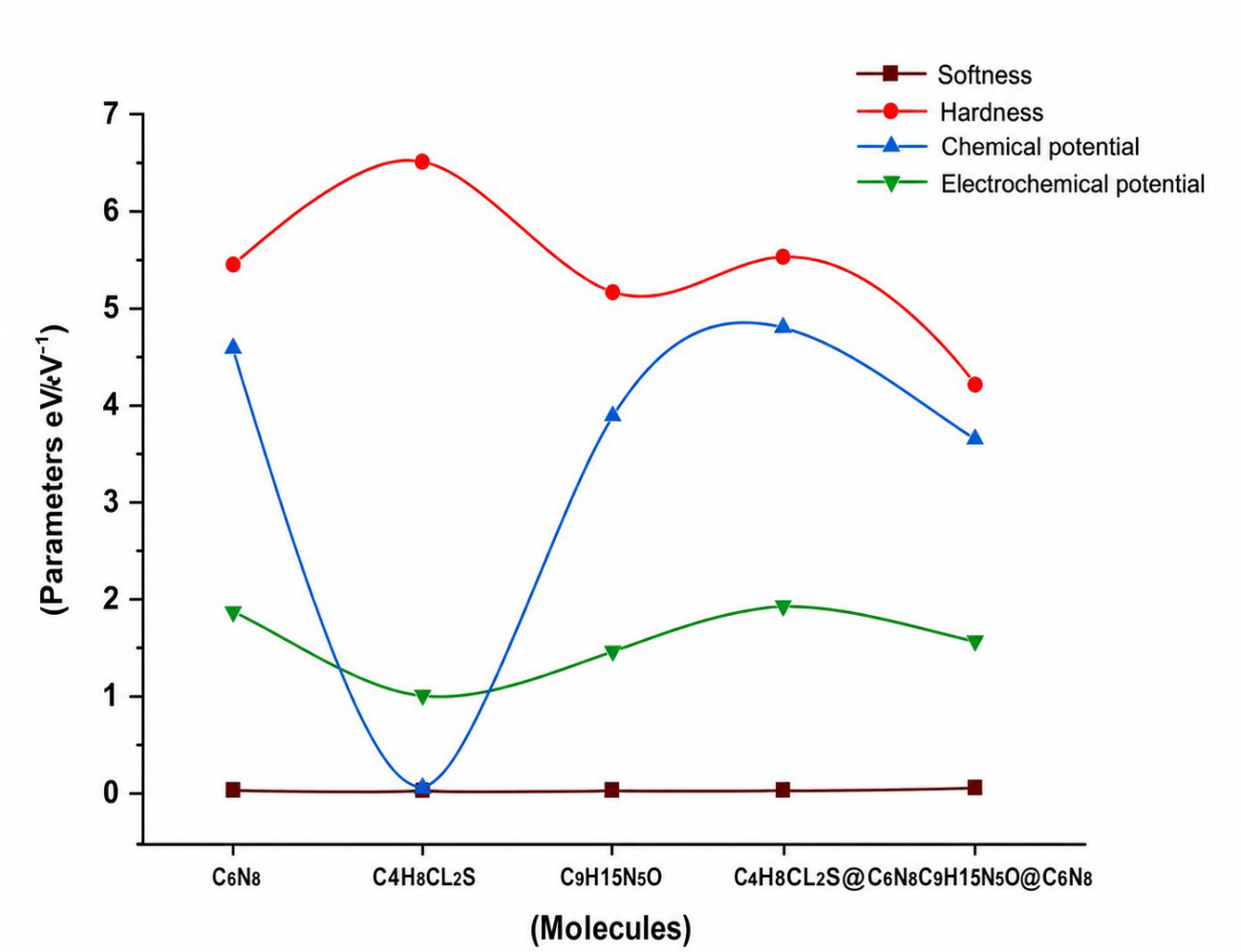

Fig. 7. Graphical representation of chemical parameters for C_6N_8, $C_4H_8Cl_2S$, $C_9H_{15}N_5O$, $C_4H_8Cl_2S@C_6N_8$, and $C_9H_{15}N_5O@C_6N_8$.

used to explore the repellent, attracting, and Van der Waals strong and weak interactions [41]. In RDG scatter spectra, which are divided into three colors, blue, green, and red, the function of $\lambda_2(r)$ varies between 0.035 and 0.000 a.u. The blue color of the maxima in the range of $\lambda_2(r) < 0$ (less than 0.01 a.u. in our example) denotes strong electrostatic forces, such as hydrogen bonding, etc. In the area where $\lambda_2(r) = 0$, which is related to the weak non-covalent attractions, such as dipole-dipole or London dispersion forces, green colour spikes occur. The red color of the peaks in the area where $\lambda_2(r) > 0$ represents steric repulsion between the atoms of the molecule [42]. The indication and the value of the sign (λ_2) ρare used to explain the type of interactions.

The overall discussion shows that both complexes ($C_4H_8Cl_2S@C_6N_8$ and $C_9H_{15}N_5O@C_6N_8$) have strong electrostatic forces (Hydrogen Bonding) between the analyte and surface, while very weak dispersion interactions (van der Waals forces).

4.4.1 3D Isosurface

In Fig. 10, 3D isosurface of $C_4H_8Cl_2S@C_6N_8$, green patches are more prominent than $C_9H_{15}N_5O@C_6N_8$, which shows the Van der Waals forces (dispersion interactions) and also shows the weak isosurface. Some portion of red and blue regions also appears in both complexes, which shows the presence of repulsion forces and hydrogen bonding, respectively.

4.4.2 Electron Localization Function (ELF)

The presence of bonding and nonbonding electrons is shown by the red color around hydrogen atoms with the greatest value, and other color shades of the ELF graph also corroborate the presence of bonding and nonbonding electrons [43] (Fig. 11). Due to the rarity of covalent bonds, high ELF values shown by the red color surrounding the atoms of hydrogen reveal a strong location of electrons. In Fig. 12 of $C_4H_8Cl_2S@C_6N_8$, nitrogen and chlorine atoms have blue circles, which represent the zone of electronic deficiency between the inside and outside layers, yet the color

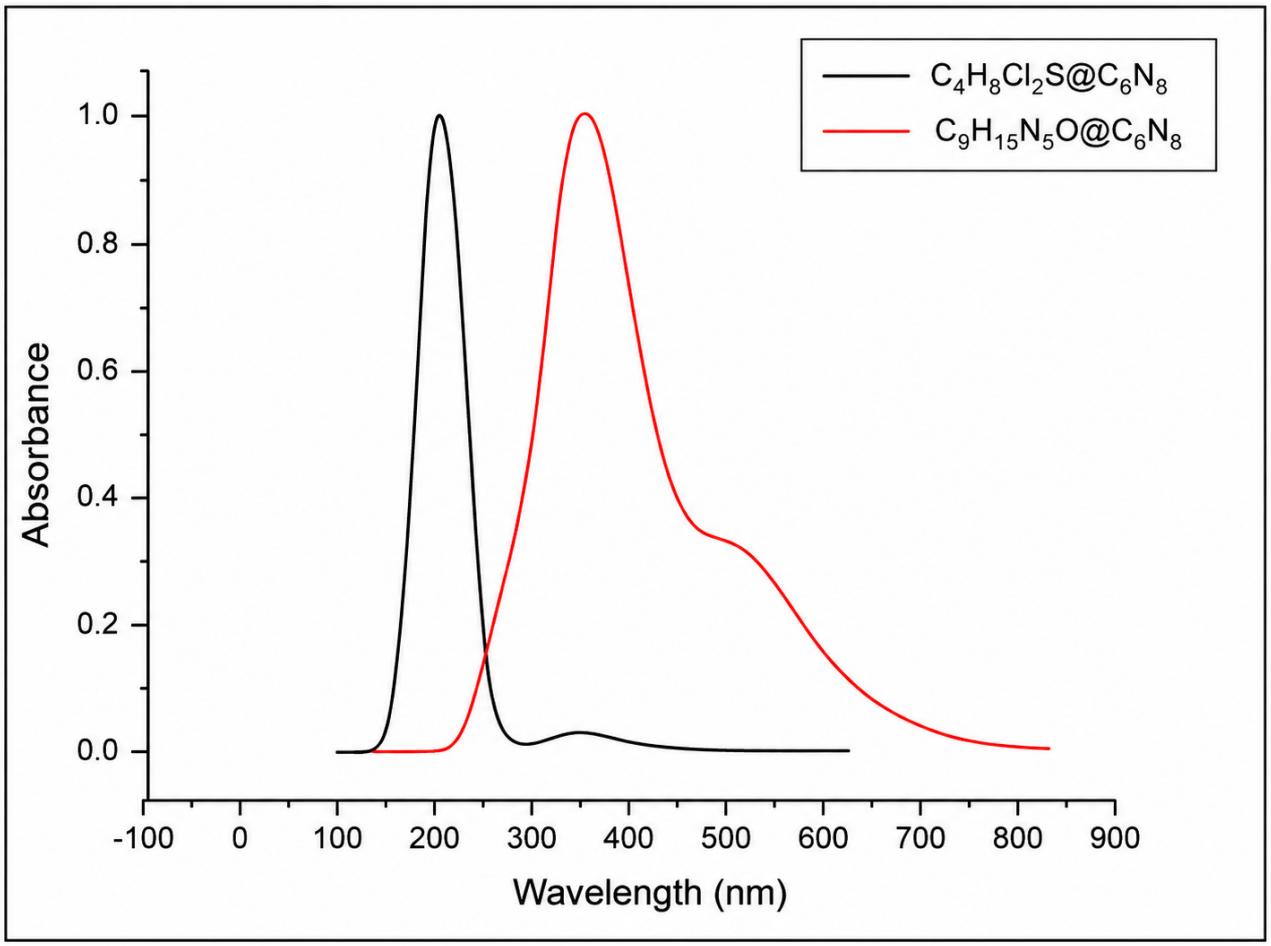

Fig. 8. UV–vis spectrum of $C_4H_8Cl_2S@C_6N_8$ and $C_9H_{15}N_5O@C_6N_8$.

blue around the carbon atoms indicates the delocalized electron cloud around this one. In both complexes, red and orange colors stand for strong electronic localization. In Fig. 12 of $C_9H_{15}N_5O@C_6N_8$, red color is more prominent [44].

4.5 Partial Density of States

In DOS and PDOS plots, the structure of fragment orbitals that are a part of molecular orbitals is demonstrated. In DOS, red, green, and color lines represent the analyte, the surface, and the total (complex). In PDOS, a bonding interaction supported the PDOS's positive value, but an anti-bonding interaction implies negative values, and non-binding interactions imply values very near to zero. The contribution of molecular orbitals is assessed by the density of states [45]. When non-spin polarized electronic band structure computations provide a high value for the density of magnetic flux, ferromagnetism is anticipated to develop. Specifically, when the Fermi level is at a strong DOS peak, states (DOS) at the Fermi level. The DOS plot represents the energy gap of 18 electrons [46].

In Fig. 13, DOS method, LUMO present on the right side, HOMO present on the left side, and the center part shows the Fermi level. In both graphs, peaks on both sides show that surface C_6N_8 acts as a donor as well as an acceptor. An analyte acts as a donor. In Fig. 14, PDOS red color shows the C_6N_8 surface, blue color shows the analyte, and black color stands for the total.

4.6 Molecular Electrostatic Potential

Molecular electrostatic potential (MEP), which is related to the electron density, is necessary to comprehend the locations for electrophilic (negative potential) and nucleophilic (nucleophilic potential) sites as well as hydrogen bonding relations [47]. The molecular electrostatic potential was calculated using an optimized structure. Fundamentally, the molecular electrostatic potential is a measure of the intensity of the neighboring charge nuclei and the electrostatic potential at a certain location. In terms of colors, the MEP discloses the molecule's size and form. Based on the interactions between electrons and protons, it is simple to determine the reactive regions of a molecule that indicate biological activity [48].

The sections of MEP that were negative (red) and positive (blue) were connected to electrophilic and nucleophilic reactivity, respectively. The electronic density is coupled to the MEP, which is a crucial descriptor for identi-

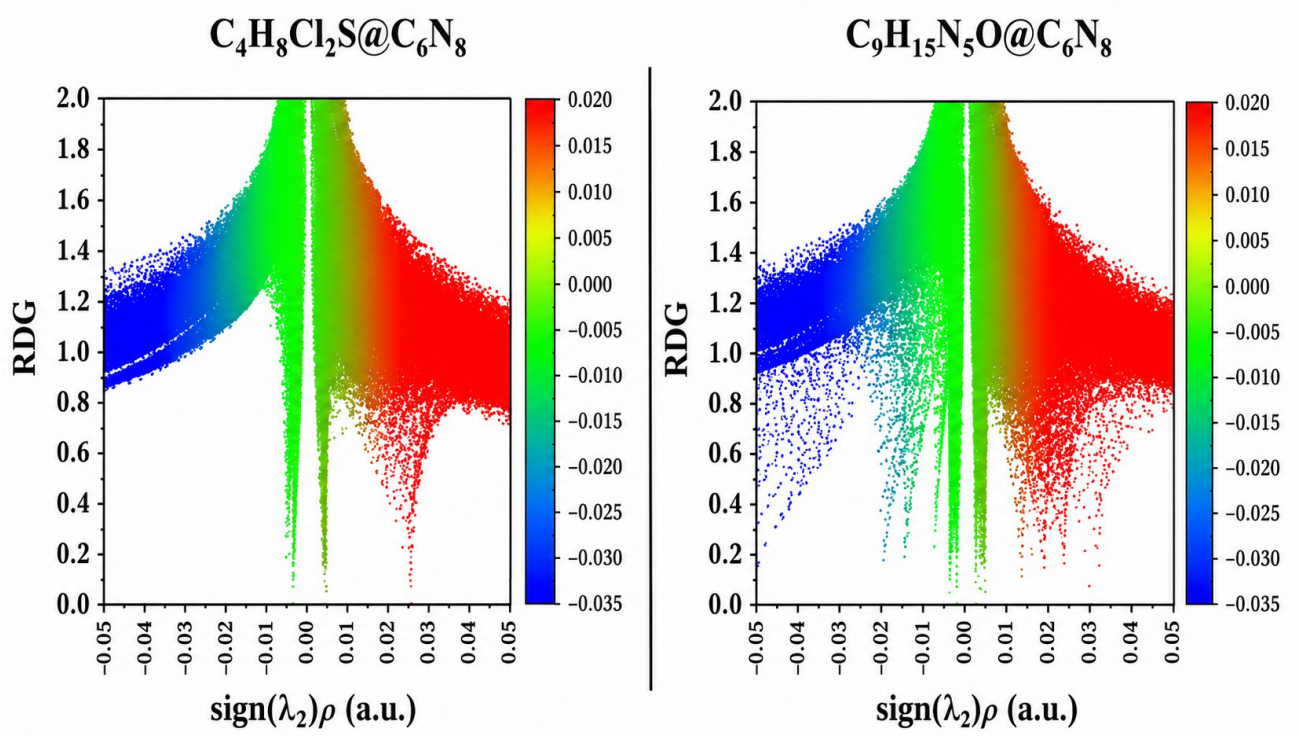

Fig. 9. Non covalent interaction (2D RDG) of complexes $C_4H_8Cl_2S@C_6N_8$ and $C_9H_{15}N_5O@C_6N_8$. RDG, reduced density gradient.

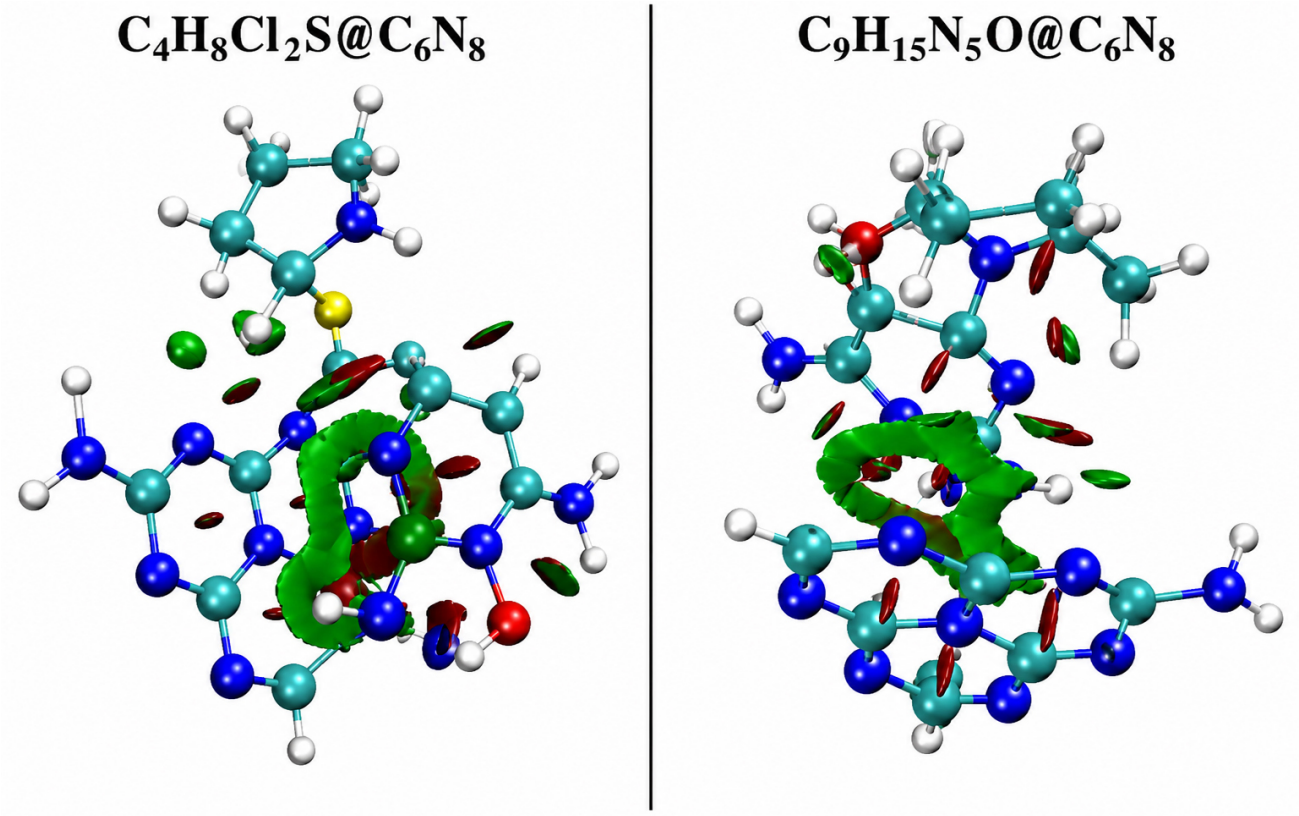

Fig. 10. 3D isosurface (van der Waals interactions) of complexes $C_4H_8Cl_2S@C_6N_8$ and $C_9H_{15}N_5O@C_6N_8$.

fying electrophilic approach, nucleophilic interactions, and hydrogen-bonding interactions [49]. The negative part of the complex $C_4H_8Cl_2S@C_6N_8$ shows the value $–6.513 \times 10^{–2}$ and is represented as the electrophilic end. The posi-

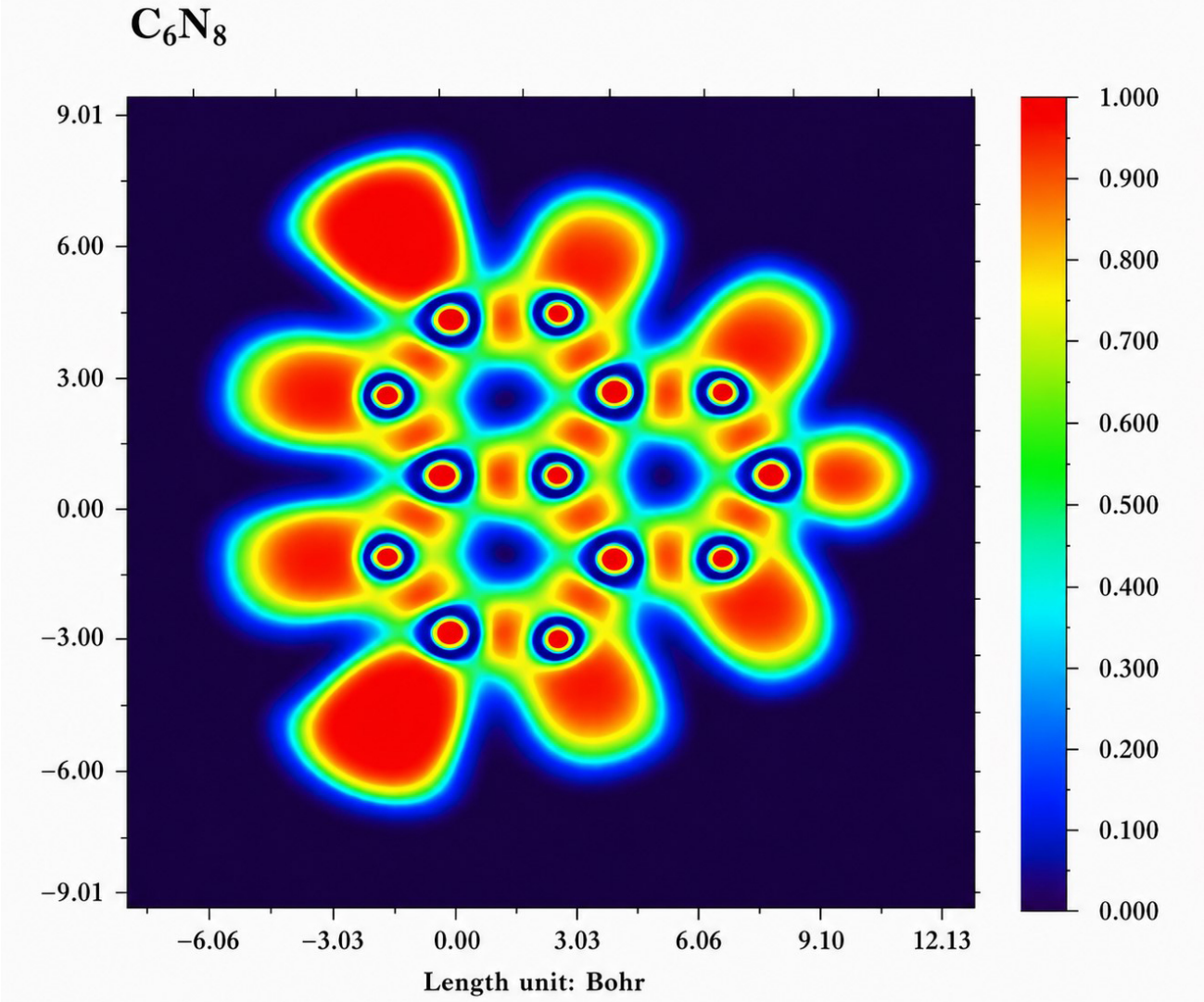

Fig. 11. Electron localization function (ELF) graph for C_6N_8.

tive part of the complex $C_4H_8Cl_2S@C_6N_8$ shows the value 6.513×10^{-2} and is represented as nucleophilic end in Fig. 15.

The electrophilic end is represented by the complex $C_9H_{15}N_5O@C_6N_8$, which has a negative component, with a value of -6.443×10^{-2}. The complex $C_9H_{15}N_5O@C_6N_8$ positive component, which is depicted as the nucleophilic end, has a value of 6.443×10^{-2} [29]. In $C_9H_{15}N_5O@C_6N_8$, red color appears, which is associated with the electrophilic attack region. In the structure of $C_4H_8Cl_2S@C_6N_8$, a light red color is present. In both complexes, the nucleophilic attack region is displayed by blue color, which is mostly present on hydrogen atoms. The region that is green-colored shows the neutral sites in the molecule.

4.7 QTAIM Analysis

Investigations on the nature of interactions according to the quantum theory of atoms in molecules are conducted. According to research, graphene and blistering chemicals interact with non-covalent energies [50]. By using QTAIM studies, the stability of the chemical structures of the title crystals has also been assessed [51]. The quantum atoms-in-molecules theory is used to examine the atomic bowl features of these molecular systems (QTAIM). According to the findings of the QTAIM study, these molecules may be divided into donor-like and acceptor-like components. The intra-molecular charge and, therefore, the energy transfer performance for each molecular system are also investigated using the local chart of the atomic electronic concentrations [52].

The bond critical point decides the type of bond that exists between an analyte and a complex bond critical point (BCP). Several topological metrics, such as the total electron energy density [H(r)], the electron density (ρ), and the Laplacian of the electron density ($\nabla^2\rho$), were used at BCPs to identify the types of interactions. At BCPs, the electron density (ρ) regulates the bond's strength, whereas the total electron energy density H(r), potential energy density V(r),

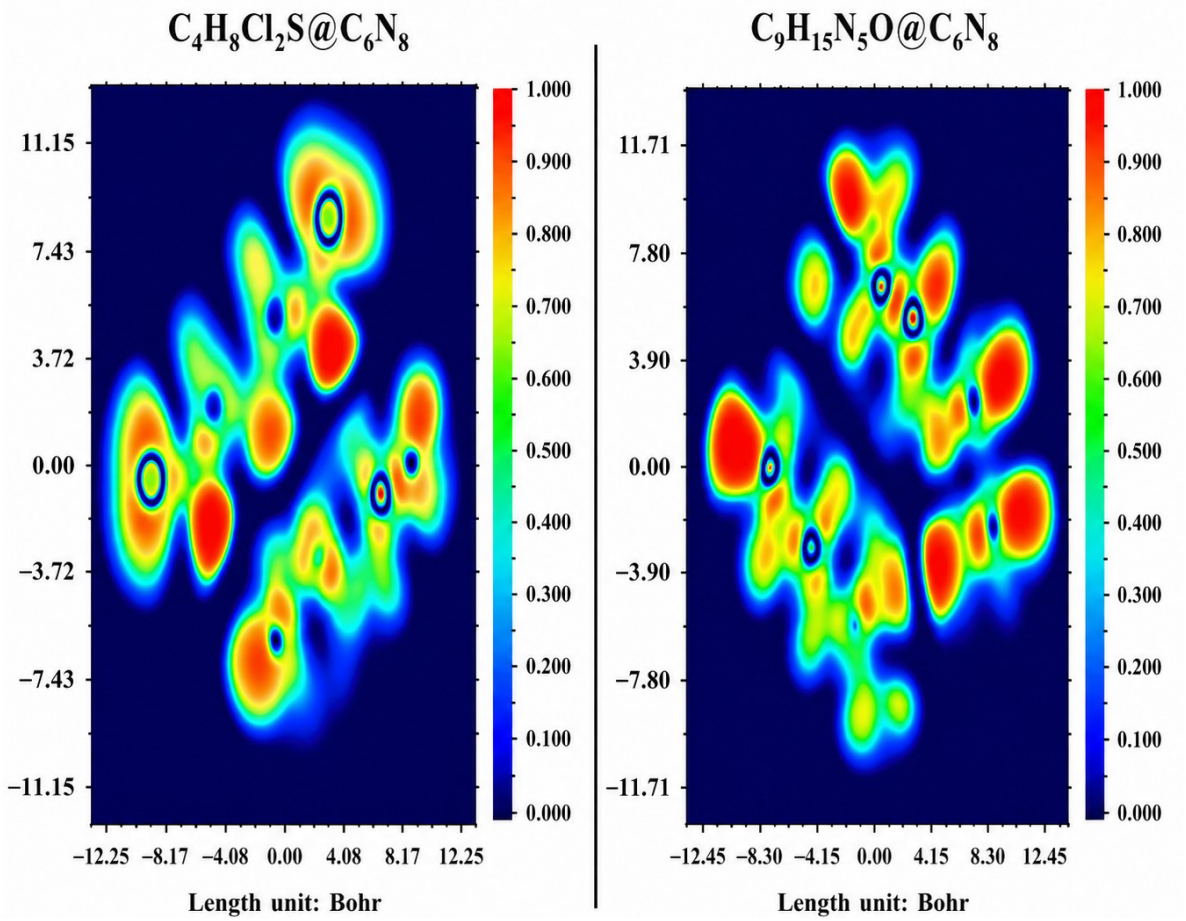

Fig. 12. Electron localization function of complexes $C_4H_8Cl_2S@C_6N_8$ and $C_9H_{15}N_5O@C_6N_8$.

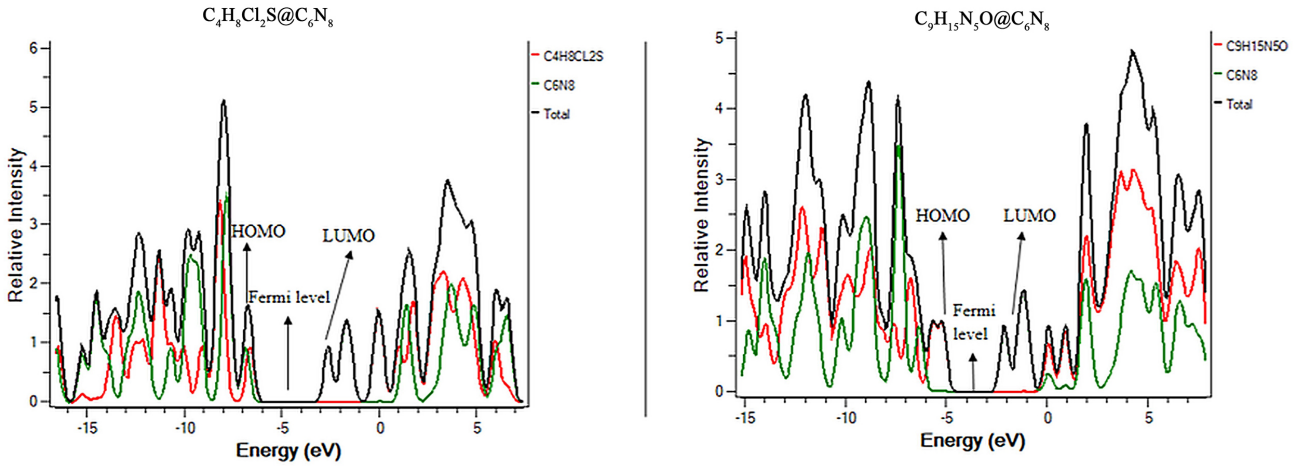

Fig. 13. Density of states of complexes $C_4H_8Cl_2S@C_6N_8$ and $C_9H_{15}N_5O@C_6N_8$.

Laplacian ($\nabla^2\rho$), and kinetic energy density G(r) evaluate the type of interactions. The existence of electrostatic interactions or hydrogen bonds is indicated by an electronic density value of >0.1, whereas the existence of weak van der Waals interactions is confirmed by a value of 0.1 (Table 1).

The values of potential energy density and kinetic energy density often stay negative and positive appropriately, at the BCPs. Adding V results in the creation of H(r) and G(r), which suggests that covalent and NCIs are present. A value of H(r) less than zero indicates the presence of covalent contacts, whereas NCIs have a value of H(r) larger than zero [53].

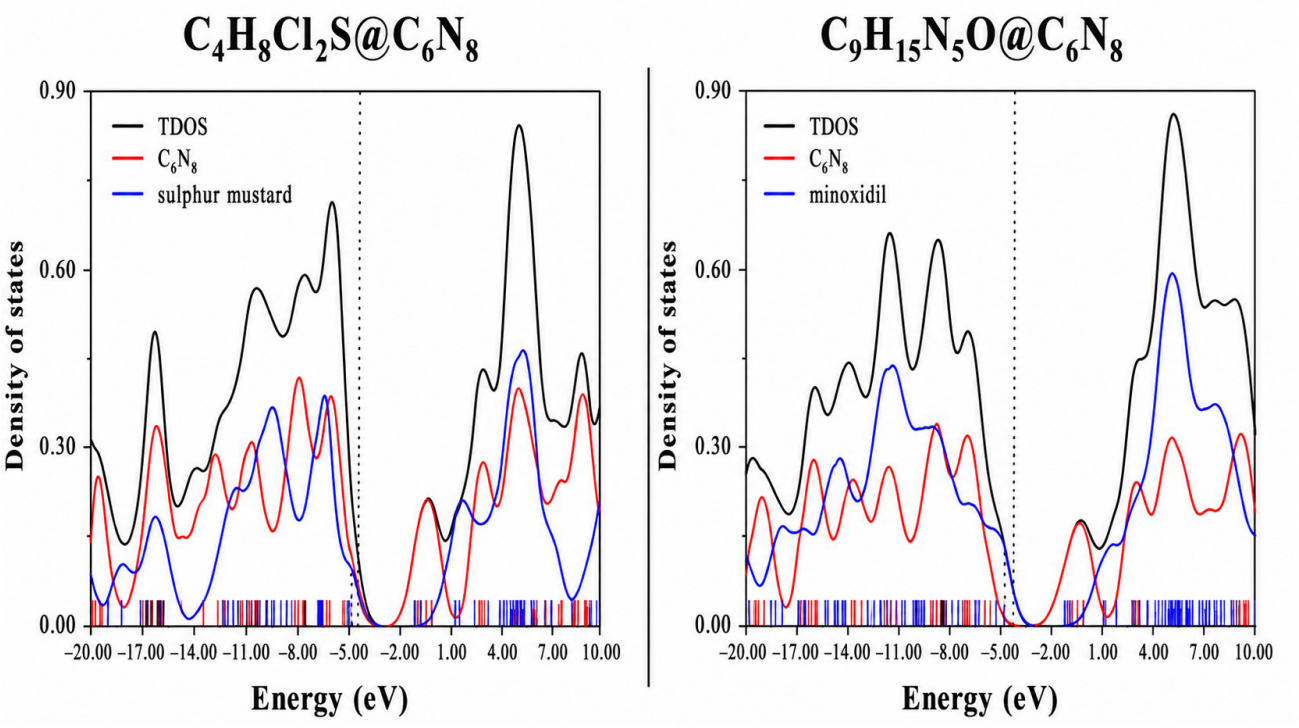

Fig. 14. Partial density of states (PDOS) of complexes $C_4H_8Cl_2S@C_6N_8$ and $C_9H_{15}N_5O@C_6N_8$.

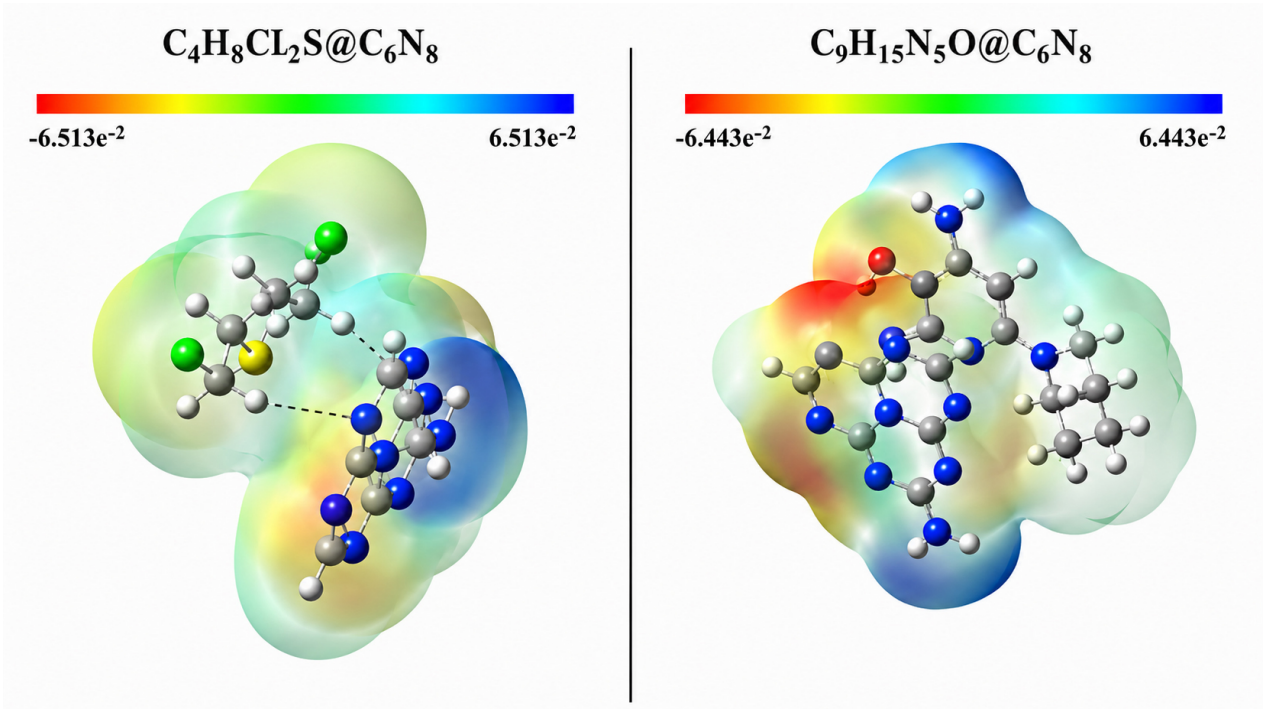

Fig. 15. Molecular electrostatic potential of complexes $C_4H_8Cl_2S@C_6N_8$ and $C_9H_{15}N_5O@C_6N_8$.

$$H(r) = G(r) + V(r) \tag{6}$$

4.8 Limitations of the Study

This study is based on density functional theory calculations. Experimental validation, solvent and temperature effects, long-term stability, and sensor fabrication aspects were not investigated and should be addressed in future work.

5. Conclusion

DFT simulations were used to calculate the adsorption of Sulphur mustard and minoxidil on the surface C_6N_8. All feasible paths of the analyte on the C_6N_8 face were investigated to obtain the best permanent shapes of the analyte@C_6N_8 complexes. $C_4H_8Cl_2S@C_6N_8$ and $C_9H_{15}N_5O@C_6N_8$ complexes exhibit adsorption energies of −30.39 and −85.34 kJ mol^{-1}, respectively. Among the two complexes, $C_9H_{15}N_5O@C_6N_8$ shows the more negative adsorption energy, indicating a stronger and more energetically favorable interaction with the C_6N_8 surface compared with $C_4H_8Cl_2S@C_6N_8$. HOMO-LUMO energy gap of (C_6N_8) changes from 4.206 to 4.007 eV in $C_4H_8Cl_2S@C_6N_8$ and decreases to 3.067 eV in $C_9H_{15}N_5O@C_6N_8$, which shows the changes in kinetic stability and chemical reactivity. The λ_{max} value for complexes $C_4H_8Cl_2S@C_6N_8$ and $C_9H_{15}N_5O@C_6N_8$ appears at 270 nm and 400 nm, respectively, in UV analysis. NCI and QTAIM analyses have also been used to investigate the intermolecular interactions. One of the most important factors in characterizing non-covalent forces is interaction energy. Interaction energy determines the stability of the molecule. The interaction energy of $C_4H_8Cl_2S@C_6N_8$ is −30.39 kJ mol^{-1}. $C_9H_{15}N_5O@C_6N_8$ is the most stable complex due to the least adsorption distance between the H-23…. N-44 atoms, which is 2.639 Å, and the highest interaction energy −85.34 kJ mol^{-1}. NBO values of $C_4H_8Cl_2S@C_6N_8$ are −0.088, and $C_9H_{15}N_5O@C_6N_8$ is -8×10^{-3}. Both negative values of complexes show the charge transfer from the surface to the analyte. The distribution of electrons and reactive sites is examined by the electron localization function. The colours (red, orange, and blue) determine the different interaction forces. The red color represents the location of electron density on the Hydrogen atom, while delocalization of electron density on the Carbon atom is highlighted by blue dots in the ELF graph. In the graph of partial density of states, red colour shows the surface, blue colour represents the analyte, and black colour represents the total or complex. The PDOS graph shows the composition of fragment orbitals participating in the molecular orbital. Molecular electrostatic potential is a computational method that uses the electron density of the compound to determine its potential reactivity. The $C_4H_8Cl_2S@C_6N_8$ complex exhibits an ultrashort recovery time of 1.001×10^{-12} s, indicating rapid desorption and excellent sensor reusability. In contrast, the $C_9H_{15}N_5O@C_6N_8$ complex has an extremely long recovery time (7.749×10^{46} s), suggesting very strong adsorption and practically irreversible binding under ambient conditions. Therefore, while C_6N_8 is highly suitable as a reusable sensor for sulphur mustard, the adsorption of $C_9H_{15}N_5O$ is more consistent with applications requiring permanent capture or removal rather than reversible sensing.

Availability of Data and Materials

Data will be made available from the corresponding authors on reasonable request.

Author Contributions

JI: Conceptualization, supervision, methodology, investigation, formal analysis, writing – original draft, writing – review and editing, project administration. HA: Investigation, data curation, formal analysis, visualization, writing – original draft preparation. HN: Investigation, methodology, validation, data curation. KA: Software, methodology, formal analysis, writing – review and editing. HAA: Conceptualization, supervision, project administration, funding acquisition, writing – review and editing. SAMA: Conceptualization, supervision, project administration, funding acquisition, writing – review and editing. All authors contributed to editorial changes in the manuscript. All authors read and approved the final manuscript. All authors have participated sufficiently in the work and agreed to be accountable for all aspects of the work.

Ethics Approval and Consent to Participate

Not applicable.

Acknowledgment

Not applicable.

Funding

This research project was funded by the Deanship of Scientific Research and Libraries, Princess Nourah bint Abdulrahman University, through the Program of Research Project Funding After Publication, grant No (RPFAP-25-1445).

Conflicts of Interest

The authors declare no conflicts of interest.

References

[1] Shehzad RA, Hussain R, Iqbal J, Ayub K. Quantum chemical study of structural, linear, and nonlinear optical response of pure silver clusters Agn (n= 2–10). Materials Science in Semiconductor Processing. 2023; 163: 107558. https://doi.org/10.1016/j.mssp.2023.107558

[2] Tahir T, Naeem N, Ans M, Rasool A, Shehzad RA, Iqbal J. Designing of difluorobenzene based donor molecules with efficient photovoltaic properties towards high performance organic solar cells. Russian Journal of Physical Chemistry A. 2022; 96: 1817–1827. https://doi.org/10.1134/S0036024422080234

[3] Shehzad RA, Zahid S, Rasool A, Iqbal J. Organic Semiconductors for Photovoltaics. Handbook of Energy Materials. Springer International Publishing: Singapore. 2026. https://doi.org/10.1007/978-981-95-2947-6_66

[4] Zhao G, Cheng Y, Wu Y, Xu X, Hao X. New 2D carbon nitride organic materials synthesis with huge-application prospects in CN photocatalyst. Small. 2018; 14: 1704138. https://doi.org/10.1002/smll.201704138

[5] Bafekry A, Stampfl C, Akgenc B, Mortazavi B, Ghergherehchi M, Nguyen CV. Embedding of atoms into the nanopore sites of the C_6N_6 and C_6N_8 porous carbon nitride monolayers with tunable electronic properties. Physical Chemistry Chemical Physics: PCCP. 2020; 22: 6418–6433. https://doi.org/10.1039/d0cp00093k

[6] Abdullahi YZ. Formation energy, mechanical and electronic properties of buckled heptazine (C6N8) sheet: First-principles calculations. Computational Condensed Matter. 2022; 30: e00619. https://doi.org/10.1016/j.cocom.2021.e00619

[7] Sarıkurt S, Ersan F. Phononic stability analysis of two-dimensional carbon nitride monolayers. Marmara Fen Bilimleri Dergisi. 2018; 30: 383–387. https://doi.org/10.7240/marufbd.399357

[8] Bafekry A, Nguyen CV, Goudarzi A, Ghergherehchi M, Shafieirad M. Investigation of strain and doping on the electronic properties of single layers of C_6N_6 and C_6N_8: a first principles study. RSC Advances. 2020; 10: 27743–27751. https://doi.org/10.1039/d0ra04463f

[9] Hussain T, Hankel M, Searles DJ. Computational evaluation of lithium-functionalized carbon nitride (g-C6N8) monolayer as an efficient hydrogen storage material. The Journal of Physical Chemistry C. 2016; 120: 25180–25188. https://doi.org/10.1021/acs.jpcc.6b06182

[10] Foo JJ, Ng SF, Xiong M, Ong WJ. Mechanistic study of the competition between carbon dioxide reduction and hydrogen evolution reaction and selectivity tuning *via* loading single-atom catalysts on graphitic carbon nitride. Nanoscale. 2024; 16: 16015–16025. https://doi.org/10.1039/d4nr01932f

[11] Feng W, Xue MJ, Zhang QL, Liu SL, Song QH. Prefluorescent probe capable of generating active sensing species in situ for detections of sulfur mustard and its simulant. Sensors and Actuators B: Chemical. 2022; 371: 132555. https://doi.org/10.1016/j.snb.2022.132555

[12] Xue MJ, Wei XZ, Feng W, Xing ZF, Liu SL, Song QH. Sensitive and selective detections of mustard gas and its analogues by 4-mercaptocoumarins as fluorescent chemosensors in both solutions and gas phase. Journal of Hazardous Materials. 2021; 416: 125789. https://doi.org/10.1016/j.jhazmat.2021.125789

[13] Ashmore MH, Nathanail CP. A critical evaluation of the implications for risk based land management of the environmental chemistry of Sulphur Mustard. Environment International. 2008; 34: 1192–1203. https://doi.org/10.1016/j.envint.2008.03.012

[14] Feng W, Li H, Xue MJ, Zhang QL, Liu SL, Song QH. Quinoline-2-thione-based fluorescent probes for selective and sensitive detections of mustard gas and its analogues. Analytica Chimica Acta. 2021; 1159: 338440. https://doi.org/10.1016/j.aca.2021.338440

[15] McNutt P. Progress towards a standardized model of ocular sulfur mustard injury for therapeutic testing. Experimental Eye Research. 2023; 228: 109395. https://doi.org/10.1016/j.exer.2023.109395

[16] Timperley CM, Forman JE, Abdollahi M, Al-Amri AS, Baulig A, Benachour D, et al. Advice on assistance and protection provided by the Scientific Advisory Board of the Organisation for the Prohibition of Chemical Weapons: Part 3. On medical care and treatment of injuries from sulfur mustard. Toxicology. 2021; 463: 152967. https://doi.org/10.1016/j.tox.2021.152967

[17] Ruiz-Medina A, Fernández-de Córdova ML, Molina-Díaz A. Integrated flow injection-solid phase spectrophotometric determination of minoxidil. Talanta. 1999; 50: 277–282. https://doi.org/10.1016/S0039-9140(99)00032-6

[18] Shamsipur M, Pashabadi A, Taherpour AA, Hemmateenejad B, Khosousi T, Parvin MH. Synthesis and characterization of glucose-capped CdSe quantum dots. Electrochemical and computational studies of corresponding carbon-ionic liquid electrode for quantitative determination of minoxidil. Journal of Electroanalytical Chemistry. 2016; 778: 116–125. https://doi.org/10.1016/j.jelechem.2016.08.030

[19] Messenger AG, Rundegren J. Minoxidil: mechanisms of action on hair growth. The British Journal of Dermatology. 2004; 150: 186–194. https://doi.org/10.1111/j.1365-2133.2004.05785.x

[20] Oliveira PM, Alencar-Silva T, Pires FQ, Cunha-Filho M, Gratieri T, Carvalho JL, et al. Nanostructured lipid carriers loaded with an association of minoxidil and latanoprost for targeted topical therapy of alopecia. European Journal of Pharmaceutics and Biopharmaceutics: Official Journal of Arbeitsgemeinschaft Fur Pharmazeutische Verfahrenstechnik E.V. 2022; 172: 78–88. https://doi.org/10.1016/j.ejpb.2022.02.003

[21] Karimian N, Gholivand MB, Taherkhani F. Computational design and development of a novel voltammetric sensor for minoxidil detection based on electropolymerized molecularly imprinted polymer. Journal of Electroanalytical Chemistry. 2015; 740: 45–52. https://doi.org/10.1016/j.jelechem.2014.12.024

[22] Ahmed H, Nadeem H, Abdelmohsen SAM, Alyousef HA, Ayub K, Iqbal J. A DFT study of carbon nitride (C6N8) as a sensing potential for phosgene (COCl2) and thionyl chloride (SOCl2) gases. Adsorption. 2025; 31: 61. https://doi.org/10.1007/s10450-025-00612-9

[23] Nadeem H, Ahmed H, Saleem U, Jamil R, Ayub K, Alsalhi SA, et al. Investigating the potential of carbon nitride as a new sensing material for NOx (N2O, N2O3, N2O4, and N2O5): a DFT study. Physica Scripta. 2024; 99: 055908. https://doi.org/10.1088/1402-4896/ad3508

[24] Sohail U, Ullah F, Mahmood T, Muhammad S, Ayub K. Adsorption of Industrial Gases (CH_4, CO_2, and CO) on Olympicene: A DFT and CCSD(T) Investigation. ACS Omega. 2022; 7: 18852–18860. https://doi.org/10.1021/acsomega.2c01796

[25] Kazachenko AS, Akman F, Abdelmoulahi H, Issaoui N, Malyar YN, Al-Dossary O, et al. Intermolecular hydrogen bonds interactions in water clusters of ammonium sulfamate: FTIR, X-ray diffraction, AIM, DFT, RDG, ELF, NBO analysis. Journal of Molecular Liquids. 2021; 342: 117475. https://doi.org/10.1016/j.molliq.2021.117475

[26] Panahi Y, Sadeghi MM. Application of metallofullerene towards adsorption of mustard gas: a detailed DFT study. Journal of Inorganic and Organometallic Polymers and Materials. 2019; 29: 1383–1389. https://doi.org/10.1007/s10904-019-01104-4

[27] Jubu PR, Obaseki OS, Nathan-Abutu A, Yam FK, Yusof Y, Ochang MB. Dispensability of the conventional Tauc's plot for accurate bandgap determination from UV–vis optical diffuse reflectance data. Results in Optics. 2022; 9: 100273. https://doi.org/10.1016/j.rio.2022.100273

[28] Ozaki Y, Morisawa Y, Ikehata A, Higashi N. Far-ultraviolet spectroscopy in the solid and liquid states: a review. Applied Spectroscopy. 2012; 66: 1–25. https://doi.org/10.1366/11-06496

[29] Nkungli NK, Ghogomu JN. Theoretical analysis of the binding of iron(III) protoporphyrin IX to 4-methoxyacetophenone thiosemicarbazone via DFT-D3, MEP, QTAIM, NCI, ELF, and LOL studies. Journal of Molecular Modeling. 2017; 23: 200. https://doi.org/10.1007/s00894-017-3370-4

[30] Tarika JDD, Dexlin XDD, Madhankumar S, Jayanthi DD, Beaula TJ. Tuning the Computational Evaluation of Spectroscopic, ELF, LOL, NCI analysis and Molecular Docking of Novel Anti COVID-19 Molecule 4-Dimethylamino Pyridinium 3, 5-Dichlorosalicylate. Spectrochimica Acta. Part A, Molecular and Biomolecular Spectroscopy. 2021; 259: 119907. https://doi.org/10.1016/j.saa.2021.119907

[31] Arulaabaranam K, Muthu S, Mani G, Ben Geoffrey AS. Speculative assessment, molecular composition, PDOS, topology exploration (ELF, LOL, RDG), ligand-protein interactions,

on 5-bromo-3-nitropyridine-2-carbonitrile. Heliyon. 2021; 7: e07061. https://doi.org/10.1016/j.heliyon.2021.e07061

[32] Gassoumi B, Dlala NA, Echabaane M, Karayel A, Özkınalı S, Castro ME, et al. Stability, spectroscopic, electrochemistry and QTAIM analysis of Cu-$Zn_{n-1}O_n$ clusters for glucose sensing application: A study on theoretical and experimental insights. Heliyon. 2022; 8: e12387. https://doi.org/10.1016/j.heliyon.2022.e12387

[33] Feitosa LF, Campos RB, Richter WE. Energetics and electronics of polar Diels-Alder reactions at the atomic level: QTAIM and IQA analyses of complete IRC paths. Journal of Molecular Graphics & Modelling. 2023; 118: 108326. https://doi.org/10.1016/j.jmgm.2022.108326

[34] Chakraborty J. An account of noncovalent interactions in homoleptic palladium(II) and platinum(II) complexes within the DFT framework: A correlation between geometries, energy components of symmetry-adapted perturbation theory and NCI descriptors. Heliyon. 2022; 8: e11408. https://doi.org/10.1016/j.heliyon.2022.e11408

[35] Jebasingh Kores J, Antony Danish I, Sasitha T, Gershom Stuart J, Jimla Pushpam E, Winfred Jebaraj J. Spectral, NBO, NLO, NCI, aromaticity and charge transfer analyses of anthracene-9,10-dicarboxaldehyde by DFT. Heliyon. 2021; 7: e08377. https://doi.org/10.1016/j.heliyon.2021.e08377

[36] Luo J, Xue ZQ, Liu WM, Wu JL, Yang ZQ. Koopmans' theorem for large molecular systems within density functional theory. The Journal of Physical Chemistry A. 2006; 110: 12005–12009. https://doi.org/10.1021/jp063669m

[37] Guin M, Halder S, Chatterjee S, Konar S. Synthesis, X-ray crystal structure of Cu (II) 1D coordination Polymer: In View of Hirshfeld surface, FMO, Molecular electrostatic potential (MEP) and Natural Bond orbital (NBO) analyses. Journal of Molecular Structure. 2022; 1270: 133949. https://doi.org/10.1016/j.molstruc.2022.133949

[38] Chaabene M, Zayer F, Agren S, Jabli M, Ghalla H, Baouab MH, et al. Use of tetraphenyl (hydroxyl) imidazole for colorimetric detection of iodide: Optical properties, computational characterizations, NBO, QTAIM, and NCI-RDG analyses. Inorganic Chemistry Communications. 2022; 144: 109917. https://doi.org/10.1016/j.inoche.2022.109917

[39] Celik S, Tanıs E. Toxic potential of poly-hexamethylene biguanide hydrochloride (PHMB): A DFT, AIM and NCI analysis study with solvent effects. Computational and Theoretical Chemistry. 2022; 1212: 113709. https://doi.org/10.1016/j.comptc.2022.113709

[40] Edet HO, Louis H, Gber TE, Idante PS, Egemonye TC, Ashishie PB, et al. Heteroatoms (B, N, S) doped quantum dots as potential drug delivery system for isoniazid: insight from DFT, NCI, and QTAIM. Heliyon. 2022; 9: e12599. https://doi.org/10.1016/j.heliyon.2022.e12599

[41] Kourat O, Djafri A, Benhalima N, Megrouss Y, Belkafouf NE, Rahmani R, et al. Synthesis, crystal structure, Hirshfeld surface analysis, spectral characterization, reduced density gradient and nonlinear optical investigation on (E)-N'-(4-nitrobenzylidene)-2-(quinolin-8-yloxy) acetohydrazide monohydrate: A combined experimental and DFT approach. Journal of Molecular Structure. 2020; 1222: 128952. https://doi.org/10.1016/j.molstruc.2020.128952

[42] Laplaza R, Peccati F, Boto A, Quan C, Carbone A, Piquemal JP, et al. NCIPLOT and the analysis of noncovalent interactions using the reduced density gradient. Wiley Interdisciplinary Reviews: Computational Molecular Science. 2021; 11: e1497. https://doi.org/10.1002/wcms.1497

[43] Hadi MA, Kelaidis N, Filippatos PP, Christopoulos SR, Chroneos A, Naqib SH, et al. Optical response, lithiation and charge transfer in Sn-based 211 MAX phases with electron localization function. Journal of Materials Research and Technology. 2022; 18: 2470–2479. https://doi.org/10.1016/j.jmrt.2022.03.083

[44] Savin A, Nesper R, Wengert S, Fässler TF. ELF: The electron localization function. Angewandte Chemie International Edition in English. 1997; 36: 1808–1832. https://doi.org/10.1002/anie.199718081

[45] Satpathi U, Deo PS. Negative partial density of states in mesoscopic systems. Annals of Physics. 2016; 375: 491–514. https://doi.org/10.1016/j.aop.2016.10.005

[46] Jung D, Koo HJ, Whangbo MH. Study of the 18-electron band gap and ferromagnetism in semi-Heusler compounds by non-spin-polarized electronic band structure calculations. Journal of Molecular Structure: THEOCHEM. 2000; 527: 113–119. https://doi.org/10.1016/S0166-1280(00)00483-8

[47] Basha F, Khan FL, Muthu S, Raja M. Computational evaluation on molecular structure (Monomer, Dimer), RDG, ELF, electronic (HOMO-LUMO, MEP) properties, and spectroscopic profiling of 8-Quinolinesulfonamide with molecular docking studies. Computational and Theoretical Chemistry. 2021; 1198: 113169. https://doi.org/10.1016/j.comptc.2021.113169

[48] Rahuman MH, Muthu S, Raajaraman BR, Raja M, Umamahesvari H. Investigations on 2-(4-Cyanophenylamino) acetic acid by FT-IR,FT-Raman, NMR and UV-Vis spectroscopy, DFT (NBO, HOMO-LUMO, MEP and Fukui function) and molecular docking studies. Heliyon. 2020; 6: e04976. https://doi.org/10.1016/j.heliyon.2020.e04976

[49] Gayathiridevi K, Deepa B, Pasupathi G. Growth, geometrical analysis, FMO, MEP UV–vis, nonlinear optical and antibacterial properties of pure and 2-furoic acid doped Guanidinium carbonate single crystal. Journal of the Indian Chemical Society. 2023; 100: 100796. https://doi.org/10.1016/j.jics.2022.100796

[50] Khan S, Sajid H, Ayub K, Mahmood T. Adsorption behaviour of chronic blistering agents on graphdiyne; excellent correlation among SAPT, reduced density gradient (RDG) and QTAIM analyses. Journal of Molecular Liquids. 2020; 316: 113860. https://doi.org/10.1016/j.molliq.2020.113860

[51] Tariq S, Khalid M, Raza AR, Rubab SL, Morais SFA, Khan MU, et al. Experimental and computational investigations of new indole derivatives: A combined spectroscopic, SC-XRD, DFT/TD-DFT and QTAIM analysis. Journal of Molecular Structure. 2020; 1207: 127803. https://doi.org/10.1016/j.molstruc.2020.127803

[52] Fallah H, Safari R, Zabolian H, Rezaei S, Moghadam M. Theoretical investigation, synthesis and fabrication of efficient organometallic light emitting diodes based on Schiff base platinum complexes: A QTAIM study. Surfaces and Interfaces. 2022; 29: 101717. https://doi.org/10.1016/j.surfin.2021.101717

[53] Gassoumi B, Dlala NA, Echabaane M, Ghalla H, Zhou Y, Castro ME, et al. Adsorption of toxic and non-toxic metals with new model of CX [4]: Experimental and computational investigation, Spectroscopic, QTAIM, and Antibacterial activity analyses. Journal of Molecular Structure. 2022; 1268: 133618. https://doi.org/10.1016/j.molstruc.2022.133618